OPEN ACCESS

Repository of the Max Delbrück Center for Molecular Medicine (MDC) in the Helmholtz Association

https://edoc.mdc-berlin.de/21474/

Rabies anterograde monosynaptic tracing allows identification of postsynaptic circuits receiving distinct somatosensory input

Pimpinella S., Sauve I., Dietrich S., Zampieri N.

This is the final version of the accepted manuscript. The original article has been published in final edited form in:

Neuroscience
2022 MAY 21 ; 491: 75-86
2022 MAR 16 (first published online: final publication)
doi: 10.1016/j.neuroscience.2022.03.011

Publisher: Elsevier / IBRO

BY-NC-ND Copyright © 2022 IBRO. Published by Elsevier Ltd. All rights reserved. This manuscript version is made available under the Creative Commons Attribution-NonCommercial-NoDerivatives 4.0 International License. To view a copy of this license, visit http://creativecommons.org/licenses/by-nc-nd/4.0/ or send a letter to Creative Commons, PO Box 1866, Mountain View, CA 94042, USA.

Rabies anterograde monosynaptic tracing allows identification of postsynaptic circuits receiving distinct somatosensory input

Sofia Pimpinella[1], Ilaria Sauve[1], Stephan Dietrich[1], and Niccolò Zampieri[1,2]

[1]Max-Delbrück-Center for Molecular Medicine Berlin-Buch,
Robert-Rössle-Str. 10, 13125 Berlin, Germany.
[2]Cluster of Excellence NeuroCure, Neuroscience Research Center,
Charité-Universitätsmedizin Berlin, Charitéplatz 1, 10117 Berlin, Germany.

Correspondance : niccolo.zampieri@mdc-berlin.de

Introduction

The somatosensory system is responsible for detecting a wide variety of sensory information and generate appropriate behavioral responses. The circuit mechanisms controlling the detection of different modalities and its transformation into motor actions are not completely understood. Much progress has been made in the characterization of primary somatosensory neurons in the peripheral nervous system and in the physiological and molecular descriptions of different subtypes specialized in the detection of discrete modalities (Abraira and Ginty, 2013; Vriens et al., 2014; Le Pichon and Chesler, 2014; Zampieri and De Nooij, 2020). However, comparatively little is known about the logic underlying the coding of sensory information and the generation of appropriate motor behaviors.

The specialization of peripheral afferents for the detection of distinct stimuli represents the foundation underlying the specificity theory, which proposes that different sensory information is encoded along parallel dedicated pathways or labelled lines (Norrsell et al, 1999). An alternative view, supported by studies on pain, is based on pattern theory and it postulates that perception is generated by temporal summation of various peripheral inputs at the level of relay centers in the central nervous system (CNS; Perl, 2007). More recently, a synergistic model, population coding, has been proposed (Ma, 2010). It suggests that cross-talk between labelled lines in the CNS is responsible for coding of sensory perception. This hypothesis highlights the functional specialization of primary sensory afferents and postulates the existence of specific patterns of connectivity with second order neurons in the spinal cord. Thus, defining the location and identity of spinal interneurons receiving input from distinct sensory modalities represent an important step toward resolving the circuit mechanisms controlling the coding of somatic sensation. However, systematic analysis has been so far precluded by the lack of high-throughput approaches that directly links the subtype identity of primary afferents with their spinal targets (Bokiniec et al., 2018). Transsynaptic tracing using rabies virus is a powerful tool for mapping neural circuits in the brain and spinal cord (Wickersham et al., 2007; Callaway and Luo, 2015). Rabies virus has also been shown to infect primary sensory neurons in the peripheral nervous system and move in the anterograde direction to spread into synaptic targets into the CNS (Ugolini, 2010; Velandia-Romero et al., 2013; Bauer et al., 2014). However, several limitations have hampered the use of rabies tracing for systematic analysis of spinal sensory circuits. First, not all sensory afferents are susceptible to infection by rabies virus (Albisetti et al., 2017). Second, neuronal transduction after peripheral, intramuscular or cutaneous, rabies injection is only efficient in neonatal mice (Stepien et al., 2010; Zampieri et al., 2014; Zhang et al., 2015). Finally, questions have been

Experimental procedures

Mouse strains

Animals were housed in the facility with controlled environmental parameters under a 12h light/ 12h dark cycle and fed with standard chow *ad libitum*. The following strains of mice of both sexes were used in this study: *PV::Cre* (Hippenmeyer et al., 2007), *TRPV1::Cre* (Mishra et al., 2011), *TRPM8::Cre* (Yarmolinsky et al., 2016), *Rosa-lsl-HTB* (Li et al.,2013) and *Rosa-lsl-tdTomato* (Ai14, Jackson Laboratory). All animal experiments were approved by the Regional Office of Health and Social Affair Berlin (LAGeSo) and performed in compliance with the German Animal Welfare Act.

Production of pseudotyped glycoprotein deficient rabies virus

RVΔG-mCherry/EnvA was produced at the Viral Core Facility (VCF) of the Charité Universitätsmedizin Berlin (https://vcf.charite.de/en/) as previously described (Wickersham et al., 2010). The virus was resuspended in PBS and viral titres were assessed by serial dilution of the virus on 293-TVA cells. For injections we used virus of titre 1 x 10^8 I.U./ml.

Spinal cord injection

For rabies tracing experiments at p9 and p30 PV^{HTB} (PV::$Cre^{+/-}$; $Rosa$-lsl-$HTB^{fl/fl}$ *x* $Rosa$-lsl-$HTB^{fl/fl}$); $TRPV1^{HTB}$ ($TRPV1$::$Cre^{+/-}$; $Rosa$-lsl-$HTB^{fl/fl}$ *x* $Rosa$-lsl-$HTB^{fl/fl}$), and $TRPM8^{HTB}$ ($TRPM8$::$Cre^{+/-}$; $Rosa$-lsl-$HTB^{fl/fl}$ *x* $Rosa$-lsl-$HTB^{fl/fl}$) mice were used. For analgesia, mice were subcutaneously injected with 5 mg/kg Carprofen 30 minutes before surgery. Anesthesia was induced with continuous inhalation of isoflurane (4% induction; 1-2% maintenance) in oxygen (1.5 %), using an isoflurane vaporizer (Parkland Scientific). A skin incision in the back was made to expose the most caudal ribs to identify the lumbar spinal cord level L1. RVΔG-mCherry/EnvA was injected in the intervertebral space starting from 300 μm deep into the dorsal horn and going back dorsally, in 6 steps consisting of 50 nl pulses (10 nl/second) every 50 μm on the left side (400 μm lateral from the midline) of the spinal cord using a 0.5 μl Hamilton syringe mounted on a UMP3 Ultra Micropump (WPI). Skin was then sutured with a nylon surgical suture. Animals were sacrificed 7 days after injection (p16 or p37).

Perfusion

Animals were anesthetized by intraperitoneal injection of 0.1 ml ketamine/xylazine mix per 10 g of weight (final concentrations: 120 mg/kg and 10 mg/kg, respectively) and checked for toe-pinch reflex before starting any procedure. Animals were transcardially perfused with ice-cold PBS until the liver was cleared of blood (~20 ml), followed by ice-cold 4% PFA (~20 ml).

Spinal cord dissection and tissue processing

Spinal cords were exposed by ventral laminectomy. Tissue was post-fixed overnight in 4% PFA at 4°C. This was followed by three washes with ice-cold PBS for 5 minutes each and overnight incubation in 30% sucrose in phosphate buffer (0.1M PB) at 4°C for cryoprotection. Samples were embedded in Optimal Cutting Temperature (O.C.T., TissueTek) compound and stored at -80°C.

Immunohistochemistry

Consecutive sections (30μm thick) were made with a Leica cryostat and mounted on Superfrost Plus slides (VWR). For immunohistochemical staining, sections were hydrated with 1X PBS for 20 minutes and permeabilized with 0.1% Triton X-100/PBS for 10 minutes at room temperature. Primary antibodies diluted in Triton X-100/PBS were incubated overnight at 4°C. Primary antibody dilutions were used as follows: rabbit anti-DsRed 1:1000 (Takara, 632496), goat anti-ChAT 1:250 (Millipore, AB144P), sheep anti-GFP 1:2000 (Bio-rad, 4745-1051), chicken anti-PV 1:10000 (de Nooij et al., 2013), sheep anti-Chx10 1:500 (Abcam, ab16141), rabbit anti-Calbindin 28k 1:2000 (SWANT, CB38), guinea pig anti-vGLUT1 1:10000 (Millipore, AB5905), goat anti-FoxP2 1:250 (Abcam, ab1307), guinea pig anti-Lbx1 1:10000 (Muller et al., 2002), guinea pig anti-PKCγ 1:500 (Cell Signaling Technology, AB 2571826), FITC conjugated-IB4 (Sigma, L2895), rabbit anti-Lhx1 1:10000 (generated by Susan Brenner-Morton in the Jessell laboratory) and rabbit anti-CGRP 1:2000 (Immunostar, 24112). After washing 3 times with Triton X-100/PBS, sections were incubated with secondary antibodies for 1 hour at room temperature. Alexa Fluor 488- and Cy3-conjugated secondary antibodies were used at 1:1000, Cy5-conjugated secondary antibodies at 1:500. Slides were coverslipped using Vectashield mounting medium. Images were acquired using a Zeiss LSM 800 confocal microscope.

Fluorescent *in situ* hybridization

For mRNA detection we used a modified RNAscope protocol from Advanced Cell Diagnostics (ACD, 322360-USM). Briefly, tissue was prepared and sectioned as described before. DRG were post-fixed in 4 % PFA (pH 7.4) at 4 °C for 15 min. After washing and dehydration (at 4 °C in 50%, 70% and 100% Ethanol), a hydrophobic barrier was created around sections. After incubation with 3% hydrogen peroxide solution at room temperature for 15 min, Protease IV treatment followed for 30 min at room temperature. *Trpv1* (313331-C2) and *Trpm8* (420451-C3) probes were dilutes 1/50 in sample diluent and hybridized for 2 hours at 40°C in a humidified chamber. For signal amplification and detection, RNAscope 2.5 HD Reagents Detection Kit-RED (ACD, 32360) was used according to the manufacturer's instructions. Immunostaining was performed as previously described and slices were mounted with ProLong Gold.

Tissue clearing

The tissue was cleared as previously described (Susaki et al., 2015). The dura from post-fixed tissue was carefully and completely removed and the spinal cord incubated at 37°C in ½ Scale CUBIC 1 with water for 3-6 hours and then incubated with Scale CUBIC 1 overnight at 37°C. On the second day, the Scale CUBIC 1 was changed with a fresh one and leaved for other 2 days. Then, samples were washed with 1X PBS overnight and incubated in ½ Scale CUBIC 2 in PBS for 3-6 hours at 37°C. The next day, samples were transferred in Pure Scale CUBIC 2 overnight at 37°C. After clearing, samples were immediately imaged a mixture of silicon- and mineral oil with a Zeiss Z1 light sheet microscope.

Neuronal position analysis

Three-dimensional positional analysis was performed as previously described (Dewitz et al., 2018). Briefly, high-resolution images of the spinal cord were processed with the imaging software IMARIS using the "spots" function to assign Cartesian coordinates to all labeled neurons. We set the central canal as the 0, 0 coordinate for the medio-lateral (x-axis) and dorso-ventral (y-axis) axes. These coordinates (x and y) were rotated and normalized to a standardized spinal cord, whose dimensions were obtained by calculating the average size of spinal cords at p16 (M-L: 800 μm, D-V: 600 μm) and p30 (M-L: 1000 μm, D-V: 600 μm), to minimize variability in size and orientation of the spinal cord between experiments. Datasets were aligned on the z-axis by starting analysis from the section where the first labeled neurons appeared (z=0) in the L1 segment and progressed caudally for more than 2 mm, covering two lumbar segments of the spinal cord. Positional analyses were performed using custom script in "R project" (R Foundation for Statistical Computing, Vienna, Austria, http://www.r-project.org). Contour and Density plot were generated using "ggplot2" package. The heat maps were used to compare the 2D spatial distribution of interneurons within each experiment and generated with the “corrplot” function. The similarity between experiments was measured by the Pearson correlation coefficient “r”.

Results

Retrograde infection of primary somatosensory neurons and anterograde transfer into second order neurons

In order to characterize the anatomical organization of spinal circuits according to the somatosensory input they receive, we combined mouse genetic and rabies virus (RV, SAD B19 strain; Wickersham et al., 2007) monosynaptic tracing techniques (Figure 1A). To achieve cellular specificity in RV infection and subsequent monosynaptic transfer we used a mouse line driving conditional expression of the TVA receptor, the RV glycoprotein (G) and a nuclear GFP reporter in combination with Cre lines targeting defined subsets of somatosensory neurons (*Rosa26*$^{Lox\text{-}stop\text{-}LoxHTB}$ or *HTB*; Li et al., 2013). Expression of the TVA receptor and G are required for selective transduction by EnvA pseudotyped G-deleted RV (RVΔG-mCherry/EnvA) and subsequent monosynaptic spreading, while the nuclear GFP reporter allows identification of starter cells (Figure 1A). We first focused on proprioceptive circuits that have been extensively characterized at anatomical and physiological levels (Balaskas et al., 2020). Thus, we crossed *parvalbumin::Cre* (*PV::Cre*), which is expressed in proprioceptive sensory neurons and a small subset of low-threshold mechanoreceptors (LTMR) with the *HTB* mouse line (Hippenmeyer et al., 2007; de Nooij et al., 2013). First, we confirmed expression specificity of the *HTB* allele and found that at lumbar levels about 96% of GFP$^+$ DRG neurons were also PV$^+$ (Figures 1B and 1C). In addition, GFP was not detected in the lumbar spinal cord up to postnatal (p) day 10, indicating that neither the TVA receptor nor G are expressed in spinal neurons at this stage (Figure S1A). In order to target sensory neurons independently of their subtype identity and peripheral target connectivity we delivered RV directly in the spinal cord to gain access to somatosensory afferents (Figure 1A). Unilateral stereotaxic injection of RVΔG-mCherry/EnvA at lumbar (L) level 1 of p9 *PV::Cre*$^{+/-}$*; HTB*$^{f/f}$ (hereafter referred to as *PV*^{HTB}) mice resulted in transduction of PV$^+$ neurons in L2-L4 DRG (Figures 1A, D, E, F, and S1B). We examined the spinal cord seven days after rabies injection and observed labeling of interneurons and motor neurons (Figure 1G and Movie 1). In contrast, when we injected *PV::Cre*$^{+/-}$*; HTB*$^{f/+}$ mice, we observed labelling of PV$^+$ DRG neurons but negligible transfer to spinal neurons (Figure S1C). This observation indicates that one copy of the *HTB* allele can promote sufficient expression of TVA to drive interaction with EnvA pseudotyped RV but not enough G to support transsynaptic transfer.

In *PV*^{HTB} experiments, we observed that the majority of neurons labeled in the spinal cord were located along or nearby the axonal trajectories of proprioceptive sensory afferents and found colocalization of rabies-driven mCherry with the presynaptic marker VGLUT1$^+$ in proximity or juxtaposed to RV$^+$ interneurons and motor neurons (Figures 1G-I; Betley et al., 2009). Altogether these data indicate that spinal injection of rabies results in retrograde labeling of proprioceptors and anterograde transsynaptic spreading into neuronal targets in the spinal cord.

Organization and identity of second order neurons receiving proprioceptive input

Next, we characterized spinal neurons labeled by rabies tracing. We generated three-dimensional maps of infected neurons and analyzed their positional organization in the spinal cord. The vast majority of second order neurons were located ipsilateral to the point of injection (Figures 2B-D, and S2). Distribution along the dorso-ventral axis presented three distinct peaks corresponding to the dorsal, intermediate, and ventral spinal cord (Figures 2B and 2D). Consistent with unbiased access to sensory afferents independent of their peripheral target, we found rabies-labelled motor neurons of both lateral and medial motor column identity in the ventral ipsilateral side (Figures 2A, 2C, and S2). The connectivity patterns obtained were qualitatively and quantitatively reproducible as shown in individual maps, distribution, and correlation analyses (“IN vs IN” $r \geq 0.9$; “MN vs MN” $r \geq 0.8$; Figures 2D, 2H, and S2). We observed variability in the amount of neuronal labelling in different experiments, however the ratio between the number of starter cells and second order neurons, defined as the “connectivity index”, remained constant indicating that, under these conditions, rabies can reproducibly label ~5 spinal neurons for each primary sensory neuron infected (Figures 2E-G and Table S1). Interestingly, a similar level of transsynaptic transfer was previously reported in retrograde tracing experiments from motor neurons using the same SAD B19 strain (Reardon et al., 2016).

In order to evaluate the possible contribution of PV$^+$ interneurons to rabies tracing experiments in PV^{HTB} mice, we assessed whether GFP$^+$ spinal neurons were labelled by rabies. We observed many GFP$^+$ neurons in p16 lumbar spinal cords consistent with reported PV expression in the spinal cord at late postnatal stages (Floyd et al., 2018). However, only few GFP$^+$; RV$^+$ neurons were found in rabies tracing experiments (Figure S3 and Table S1). This data, along with the absence of GFP labeling in the spinal cord of PV^{HTB} mice one day after rabies injection, suggest that GFP$^+$; RV$^+$ neurons represent second order cells and therefore are not likely to contribute to transsynaptic tracing. Next, we investigated the identity of spinal neurons labelled by rabies virus. In addition to motor neurons, several cardinal classes of spinal neurons are known to receive direct proprioceptive input (Eccles et al., 1957; Côté et al., 2018).

We analysed the expression of markers that, along with positional information, define V2a, V1, V0, and dI4 identities at early postnatal stages (Bikoff et al., 2016). We found rabies labelled Chx10^{+} V2a interneurons, FoxP2^{+} V1 interneurons, ventrally positioned calbindin^{+} Renshaw cells, and Lhx1^{+}interneurons whose dorsal position is suggestive of dI4/dILB identity (Figure 3). These findings confirm that rabies labels spinal neurons that are known to receive monosynaptic proprioceptive input and therefore represent genuine postsynaptic targets (Zampieri et al., 2014).

Anterograde tracing from thermosensitive neurons

In order to explore the overall organization of spinal somatosensory circuits we mapped post-sensory neurons receiving input from different primary afferents. Since the *PV::Cre* line gives access to neurons of mechanoreceptive lineage, mainly proprioceptors and a small subset of LTMR, we decided to focus on thermosensation, a distinct modality that is accessible using available mouse genetic tools. We took advantage of the *TRPV1::Cre* and *TRPM8::Cre* mouse lines that are known to target DRG neurons that detect thermal stimuli (Mishra et al., 2011; Yarmolinsky et al., 2016). *TRPV1* is transiently expressed during development by sensory neurons dedicated to the detection of thermal stimuli, thus labeling all thermosensitive neurons in lineage tracing experiments; in contrast, *TRPM8* expression has been shown to be restricted to a small subset of cold-sensing neurons (Dhaka et al., 2008; Mishra et al., 2011; Yarmolinsky et al., 2016). Indeed, GFP expression in *TRPV1::Cre*$^{+/-}$*; HTB*$^{f/f}$ and *TRPM8::Cre* $^{+/-}$*; HTB*$^{f/f}$ (hereafter referred to as *TRPV1*^{HTB} and *TRPM8*^{HTB}) mice revealed a clear difference in DRG labeling (Figures 4A and 4B). This observation was confirmed by tracing sensory afferents in *TRPV1::Cre*$^{+/-}$*; Ai14*$^{f/+}$ mice , where we found dense staining in the dorsal spinal cord while only sparse signal was detected in the case of *TRPM8::Cre*$^{+/-}$*; Ai14*$^{f/+}$ (Figures S4A and S4B). In addition, we assessed *Trpv1* and *Trpm8* expression in GFP^{+} neurons from *TRPV1*^{HTB} mice by using fluorescent *in situ* hybridization. As previously reported, we found that lineage tracing with *TRPV1::Cre* captures not only *Trpv1*$^{+}$ (~ 40% of GFP^{+} cells) but also *Trpm8* $^{+}$ (~ 10% of GFP^{+} cells) and a small fraction of *Trpv1*$^{+}$; *Trpm8* $^{+}$ neurons (Figures S4C and S4D; Mishra et al., 2011). Finally, we did not observe labeling of spinal neurons with either *TRPV1::Cre* or *TRPM8::Cre* (Figures 4E, 4F, S4A, and S4B).

As previously done for *PV*^{HTB} experiments, we performed L1 unilateral stereotaxic injection of RVΔG-mCherry/EnvA in p9 mice and performed analysis at p16. In both cases we obtained selective infection of GFP^{+} DRG neurons (Figures 4A-C). We observed similar efficiencies in primary transduction, however, because of the different abundance of sensory neurons expressing Cre in the *TRPV1::Cre* and *TRPM8::Cre* lines, the number of starter cells was much higher in *TRPV1*^{HTB} experiments (Figure 4A, 4B, 4D, 4I, and Table S1). Surprisingly, we did not observe a proportional increase in the number of second order neurons labeled in *TRPV1*^{HTB} mice, thus resulting in a low connectivity index (Figures 4I-K and Table S1). Next, we examined the spinal cords and found extensive labeling on the ipsilateral side with higher incidence of RV^{+} neurons in the dorsal horn that sharply decreased in the intermediate and ventral areas (Figures 4E-H). The spatial organization of RV^{+} neurons in *TRPV1*^{HTB} and *TRPM8*^{HTB} experiments were qualitatively similar and injections reproducible, as shown by single maps, distribution, and correlation analyses (Figures S4E and S4F). Next, we assessed whether wiring of these spinal circuits changes over postnatal development and performed rabies injection in p30 *TRPV1*^{HTB} and *TRPM8*^{HTB} mice and analyzed spinal cords at p37. In both cases, we observed spatial distributions comparable to the one observed at p16, thus indicating that the overall organization of spinal interneurons receiving thermal information is preserved from early postnatal development (Figure S5). Altogether, these data show that rabies can be used to trace from distinct primary somatosensory neuron subtypes at postnatal and adult stages

Organization of post-sensory circuits in the dorsal laminae of the spinal cord

Recent studies demonstrated the importance of topographic organization of dorsal spinal interneurons for encoding motor reflexes mediated by different noxious stimuli (Gatto et al., 2021; Peirs et al., 2021). Thus, we asked whether the distribution of neurons labelled in *PV*^{HTB}, *TRPV1*^{HTB}, and *TRPM8*^{HTB} may provide insights into the anatomical basis for the functional specificity of spinal somatosensory circuits. In *PV*^{HTB} experiments we found 43% of rabies-labeled neurons in the intermediate spinal cord (defined as the dorso-ventral area from 0 to 300μm) and a similar number of cells in the ventral (23%; 0 to -600μm) and dorsal (29%; 300 to 600μm) areas (Figure 5A). In contrast, the majority of neurons traced after rabies injections in *TRPV1*^{HTB} and *TRPM8*^{HTB} mice were located in the dorsal spinal cord (Figure 5A; *TRPV1*^{HTB} = 78% and *TRPM8*^{HTB} = 65%). Correlation analysis confirmed this observation by showing that Cartesian coordinates of RV^{+} neurons in *TRPV1*^{HTB} and *TRPM8*^{HTB} experiments highly correlate with each other but not with the ones from *PV*^{HTB} ("*TRPV1*^{HTB} vs *TRPM8*^{HTB}" $r \geq 0.85$; "*TRPV1*^{HTB}or *TRPM8*^{HTB} vs *PV*^{HTB}" $r \leq 0.55$; Figure 5B). Despite the broad dorso-ventral segregation of neurons receiving thermal and mechanical information, an area of potential overlap is evident in the dorsal horn, where neurons labelled in *PV*^{HTB} present prominent laminar distribution (Figures 2B, 2D and 5A).

We used staining for CGRP and PKCγ, markers for lamina I-IIo and IIi-III, as an internal reference for assessing relative positioning of dorsal interneurons labelled in *PV*^{HTB}, *TRPV1*^{HTB}, and *TRPM8*^{HTB} experiments (Polgar et al., 1999). The data indicate that in *PV*^{HTB} experiments RV^{+} neurons are rarely found above lamina IIi, as opposed to *TRPV1*^{HTB} mice where RV^{+} neurons are located mostly in lamina I and IIo, largely overlapping with the CGRP termination zone (Figures 5C-F). In addition, neurons receiving mechanical information, captured in *PV*^{HTB} experiments, display a prominent laminar positioning mostly overlapping with PKCγ labeling, an area known to receive extensive input from cutaneous LTMR (Figures 5C, 5D, and 5E; Abraira et al., 2017). Spinal neurons traced in *TRPM8*^{HTB} mice presented a more homogenous distribution across dorsal layers, with about half of the neurons found in laminae I-IIo and half in laminae IIi-III (Figures 5F and 5G). Altogether, these data indicate that interneurons residing in the superficial laminae can be divided into different, partially overlapping populations of neurons according to the sensory input they receive (Figure S4G).

Discussion

In order to better understand the functional organization of spinal circuits controlling the processing of sensory information, it is critical to determine the patterns of connectivity between distinct primary sensory neuron subtypes and their targets in the central nervous system. In this study, by combining mouse genetics and rabies monosynaptic tracing we describe a method to directly link sensory input from defined, modality specific, primary afferents to neuronal targets in the spinal cord and analyze the anatomical organization of spinal circuits encoding mechanical and thermal information.

The approach takes advantage of the ability of primary sensory neurons to support rabies transsynaptic transfer in the anterograde direction (Ugolini, 2010; Velandia-Romero et al., 2013; Bauer et al., 2014; Zampieri et al., 2014). In contrast to previous studies that used peripheral delivery of rabies virus to infect sensory neurons through their terminals, we opted for stereotaxic injection of EnvA pseudotyped rabies virus in the spinal cord to infect TVA-expressing neurons through their central afferents. This route has two advantages. First, the efficiency of rabies transduction of DRG neurons, via their peripheral terminals is known to decrease rapidly within the first neonatal days, essentially preventing the use of this route after p4 (Zampieri et al., 2014; Zhang et al., 2015). This limitation does not apply to intraspinal injection, thus opening the way for studying the organization of spinal post-sensory circuits during and after postnatal development in physiological or disease models. Second, intraspinal injection allows unbiased access to all sensory afferents projecting at a desired spinal level independent of their identity or pattern of peripheral innervation (i.e.: hairy vs glabrous skin, cutaneous vs muscle, etc.), in principle allowing comparisons of post-sensory circuits from different modalities without any limitation.

We used a mouse genetic strategy to specify starter cells by driving conditional expression of the TVA receptor, G protein, and a reporter under control of Cre recombinase. This is an effective and relatively simple method for driving transgene expression in all neurons of interest. However, it requires a high degree of specificity in the Cre line, otherwise transient or leaky expression could result in the generation of multiple sets of cells capable of supporting rabies transsynaptic tracing. For this reason, we carefully analyzed the patterns of the reporter expression in the DRG and spinal cords of the Cre lines employed in this study and choose to inject at p9 before we could observe labeling of spinal interneurons in *PV::Cre*. In order to ensure stringent specificity alternative strategies, using inducible Cre lines, intersectional genetic, and viral approaches can be implemented. For example, complementation of TVA and G expression using peripheral AAV injection in combination with rabies intraspinal delivery could eliminate specificity issues common to many Cre lines, as in the case of expression *PV::Cre* in spinal interneurons.

In agreement with a previous report, we did not find any obvious restriction in the ability of EnvA-pseudotyped rabies virus to infect TVA expressing somatosensory neuron (Albisetti et al., 2017). However, in comparison to TRPM8 and PV experiments, we observed a low connectivity index when tracing from *TRPV1*^{HTB} mice. Our data do not allow to distinguish whether this observation reflects an intrinsic property of these circuits or could hint at a limited ability of a subset of *TRPV1::Cre* neurons to support rabies spreading. It has been suggested that neural activity may have an important role in promoting efficient rabies transsynaptic transfer. Many nociceptors are labelled with *TRPV1::Cre* and because of the controlled conditions of laboratory mouse housing these cells are mostly not actively firing, thus possibly limiting their contributions to rabies tracing. A similar scarcity in connectivity has been previously shown in tracing experiments from *TRPV1::Cre* sensory neurons after rabies cutaneous injection (Zhang et al., 2015). The authors interpreted their results as an indication that transsynaptic labeling from sensory neurons represents retrograde transfer into presynaptic neurons through relatively infrequent axo-axonic synapses instead of anterograde transfer into postsynaptic targets (Zhang et al., 2015). Analysis of neuronal identity and position in *PV*^{HTB} experiments strongly support anterograde transfer into postsynaptic targets, as we consistently observe labeling of motor neurons and spinal interneurons that are well-known recipients of monosynaptic input from proprioceptive sensory afferents (Eccles et al., 1957; Zampieri et al., 2014; Bikoff et al., 2016; Côté et al., 2018).

In order to assess the overall anatomical organization of spinal somatosensory circuits, we used three different mouse lines. *PV::Cre,* targeting mechanosensitive neurons, proprioceptors and a small subset of LTMR; *TRPV1::Cre,* targeting a wide cohort of somatosensory neurons mainly of thermosensitive lineage; *TRPM8::Cre,* targeting cold-sensing neurons (Hippenmeyer et al., 2007; Dhaka et al., 2008; Mishra et al., 2011; de Nooij et al., 2013; Yarmolinsky et al., 2016). We were therefore able to map neurons involved in the detection of two different stimulus modalities, proprioception and thermosensation, as well as circuits for more defined sensory features, a minority of cutaneous mechanoreceptors and cold sensing neurons. Positional analysis of post-sensory neurons revealed shared and distinct features of spinal somatosensory circuits. First, in all cases analyzed, we observed a very prominent ipsilateral bias in connectivity, with very limited labeling of contralateral neurons, indicating that the first relay stations in the spinal cord processing somatic sensation do not directly integrate information coming from both sides of the body. Second, post-sensory neurons receiving mechanical and thermal information are mostly segregated along the dorso-ventral axis highlighting the functional separation of the dorsal and ventral spinal cord for sensory processing and motor control, respectively. Third, at a finer level of resolution, the anatomical organization of post-sensory circuits in the dorsal horn reflects the recently described functional specialization of superficial spinal interneurons in laminae I-IIo for encoding reflexes mediated by inflammatory and noxious stimuli, and of deeper interneurons in laminae IIi-IV for sensory-motor behaviours driven by mechanical inputs (Gatto et al., 2021; Peirs et al., 2021). Interneurons labeled in *TRPV1*^{HTB} experiments, which captures all thermosensitive afferents including nociceptors, are present at higher density in lamina I and IIo, mostly segregated from the ones traced in *PV*^{HTB} experiments, representing inputs relaying proprioceptive and a small part of cutaneous mechanoreceptive information, that are found in deeper layers starting from lamina IIi. Interestingly, spinal targets of afferents traced in *TRPM8*^{HTB} experiments, that detect cold sensation, are not biased toward more superficial laminae and present a more homogenous distribution throughout the dorsal horn. Altogether, these findings support a population coding model where different, modality specific, sensory inputs converge on ensembles of spinal interneurons that present stereotyped spatial organization and control different sensory-motor functions (Gradwell and Abraira, 2021).

Acknowledgements

We would like to thank Mark Hoon (NIH, USA) for generously providing the *TRPV1::Cre* and *TRPM8::Cre* mouse lines; Martyn Goulding (Salk Institute, USA) for the *Rosa-lsl-HTB* mouse line. Carmen Birchmeier for generously sharing the anti CGRP antibody, Susan Brenner-Morton for the anti Lhx1 antibody. Liana Kosizki for technical assistance and the MDC Advanced Light Microscope facility for assistance with image acquisition and analysis. We are grateful to Marco Beato, Jay Bikoff, Joriene de Nooij, Andrew Murray, James Poulet and members of the Zampieri laboratory for comments on the manuscript. N.Z. was supported by the DFG (ZA 885/1-1, ZA885/2-1, and EXC 257 NeuroCure).

References

Abraira, V.E., and Ginty, D.D. (2013). The Sensory Neurons of Touch. Neuron *79*, 618–639.

Abraira, V.E., Kuehn, E.D., Chirila, A.M., Springel, M.W., Toliver, A.A., Zimmerman, A.L., Orefice, L.L., Boyle, K.A., Bai, L., Song, B.J., et al. (2017). The Cellular and Synaptic Architecture of the Mechanosensory Dorsal Horn. Cell *168*, 295-310.e19.

Albisetti, G.W., Ghanem, A., Foster, E., Conzelmann, K.-K., Zeilhofer, H.U., and Wildner, H. (2017). Identification of Two Classes of Somatosensory Neurons That Display Resistance to Retrograde Infection by Rabies Virus. J. Neurosci. *37*, 10358–1037.

Balaskas, N., Ng, D., and Zampieri, N. (2020). The Positional Logic of Sensory-Motor Reflex Circuit Assembly. Neuroscience *450*, 142–150.

Bauer, A., Nolden, T., Schroter, J., Romer-Oberdorfer, A., Gluska, S., Perlson, E., and Finke, S. (2014). Anterograde Glycoprotein-Dependent Transport of Newly Generated Rabies Virus in Dorsal Root Ganglion Neurons. J. Virol. 88, 14172–14183.

Betley, J.N., Wright, C.V.E., Kawaguchi, Y., Erdélyi, F., Szabó, G., Jessell, T.M., and Kaltschmidt, J.A. (2009). Stringent Specificity in the Construction of a GABAergic Presynaptic Inhibitory Circuit. Cell 139, 161–174.

Bikoff, J.B., Gabitto, M.I., Rivard, A.F., Drobac, E., MacHado, T.A., Miri, A., Brenner-Morton, S., Famojure, E., Diaz, C., Alvarez, F.J., et al. (2016). Spinal Inhibitory Interneuron Diversity Delineates Variant Motor Microcircuits. Cell *165*, 207–219.

Bokiniec, P., Zampieri, N., Lewin, G.R., and Poulet, J.F. (2018). The neural circuits of thermal perception. Curr. Opin. Neurobiol. 52, 98–106.

Callaway, E.M., and Luo, L. (2015). Monosynaptic Circuit Tracing with Glycoprotein-Deleted Rabies Viruses. J. Neurosci. *35*, 8979–8985.

Côté, M.-P., Murray, L.M., and Knikou, M. (2018). Spinal Control of Locomotion: Individual Neurons, Their Circuits and Functions. Front. Physiol. *9*, 1–27.

de Nooij, J.C., Doobar, S., and Jessell, T.M. (2013). Etv1 Inactivation Reveals Proprioceptor Subclasses that Reflect the Level of NT3 Expression in Muscle Targets. Neuron *77*, 1055–1068.

Dewitz, C., Pimpinella, S., Hackel, P., Akalin, A., Jessell, T.M., Zampieri, N., 2018. Nuclear Organization in the Spinal Cord Depends on Motor Neuron Lamination Orchestrated by Catenin and Afadin Function. Cell Rep. 22, 1681–1694.

Dhaka, A., Earley, T.J., Watson, J., and Patapoutian, A. (2008). Visualizing Cold Spots: TRPM8-Expressing Sensory Neurons and Their Projections. J. Neurosci. *28*, 566–575.

Eccles, J.C., Eccles, R.M., and Lundberg, A. (1957). The convergence of monosynaptic excitatory afferents on to many different species of alpha motoneurones. J. Physiol. *137*, 22–50.

Floyd, T.L., Dai, Y., and Ladle, D.R. (2018). Characterization of calbindin D28k expressing interneurons in the ventral horn of the mouse spinal cord. Dev. Dyn. 247, 185–193.

Gatto, G., Bourane, S., Ren, X., Di Costanzo, S., Fenton, P.K., Halder, P., Seal, R.P., and Goulding, M.D. (2021). A Functional Topographic Map for Spinal Sensorimotor Reflexes. Neuron 109, 91-104.e5.

Gradwell, M.A., and Abraira, V.E. (2021). Sensory Symphonies: How Excitatory Spinal Cord Modules Orchestrate Behavior. Neuron 109, 3–5.

Hippenmeyer, S., Huber, R.M., Ladle, D.R., Murphy, K., and Arber, S. (2007). ETS Transcription Factor Erm Controls Subsynaptic Gene Expression in Skeletal Muscles. Neuron *55*, 726–740.

Koch, S.C., Acton, D., and Goulding, M. (2018). Spinal Circuits for Touch, Pain, and Itch. Annu. Rev. Physiol. *80*, 189–217.

Lallemend, F., and Ernfors, P. (2012). Molecular interactions underlying the specification of sensory neurons. Trends Neurosci. *35*, 373–381.

Le Pichon, C.E., and Chesler, A.T. (2014). The functional and anatomical dissection of somatosensory subpopulations using mouse genetics. Front. Neuroanat. *8*, 21.

Li, Y., Stam, F.J., Aimone, J.B., Goulding, M., Callaway, E.M., and Gage, F.H. (2013). Molecular layer perforant path-associated cells contribute to feed-forward inhibition in the adult dentate gyrus. Proc. Natl. Acad. Sci. *110*, 9106–9111.

Ma, Q. (2010). Labeled lines meet and talk: Population coding of somatic sensations. J. Clin. Invest. *120*, 3773–3778.

Mishra, S.K., Tisel, S.M., Orestes, P., Bhangoo, S.K., and Hoon, M.A. (2011). TRPV1-lineage neurons are required for thermal sensation. EMBO J. *30*, 582–593.

Müller, T., Brohmann, H., Pierani, A., Heppenstall, P.A., Lewin, G.R., Jessell, T.M., Birchmeier, C., 2002. The homeodomain factor lbx1 distinguishes two major programs of neuronal differentiation in the dorsal spinal cord. Neuron 34, 551–62.

Norrsell, U., Finger, S., and Lajonchere, C. (1999). Cutaneous sensory spots and the “law of specific nerve energies”: history and development of ideas. Brain Res. Bull. 48, 457–465.

Peirs, C., Williams, S.-P.G., Zhao, X., Arokiaraj, C.M., Ferreira, D.W., Noh, M., Smith, K.M., Halder, P., Corrigan, K.A., Gedeon, J.Y., et al. (2021). Mechanical Allodynia Circuitry in the Dorsal Horn Is Defined by the Nature of the Injury. Neuron 109, 73-90.e7.

Perl, E.R. (2007). Ideas about pain, a historical view. Nat. Rev. Neurosci. 8, 71–80.

Polgár, E., Fowler, J.., McGill, M.., and Todd, A.. (1999). The types of neuron which contain protein kinase C gamma in rat spinal cord. Brain Res. *833*, 71–80.

Reardon, T.R., Murray, A.J., Turi, G.F., Wirblich, C., Croce, K.R., Schnell, M.J., Jessell, T.M., and Losonczy, A. (2016). Rabies Virus CVS-N2c ΔG Strain Enhances Retrograde Synaptic Transfer and Neuronal Viability. Neuron 89, 711–724.

Stepien, A.E., Tripodi, M., and Arber, S. (2010). Monosynaptic rabies virus reveals premotor network organization and synaptic specificity of cholinergic partition cells. Neuron *68*, 456–472.

Sürmeli, G.G., Akay, T., Ippolito, G.C., Tucker, P.W., Jessell, T.M., 2011. Patterns of spinal sensory-motor connectivity prescribed by a dorsoventral positional template. Cell 147, 653–65.

Susaki, E.A., Tainaka, K., Perrin, D., Yukinaga, H., Kuno, A., and Ueda, H.R. (2015). Advanced CUBIC protocols for whole-brain and whole-body clearing and imaging. Nat. Protoc. 10, 1709–1727.

Ugolini, G. (2010). Advances in viral transneuronal tracing. J. Neurosci. Methods 194, 2–20.

Velandia-Romero, M.L., Castellanos, J.E., and Martínez-Gutiérrez, M. (2013). In vivo differential susceptibility of sensory neurons to rabies virus infection. J. Neurovirol. 367–375.

Vriens, J., Nilius, B., and Voets, T. (2014). Peripheral thermosensation in mammals. Nat. Rev. Neurosci. *15*, 573–589.

Wickersham, I.R., Lyon, D.C., Barnard, R.J.O., Mori, T., Finke, S., Conzelmann, K.-K., Young, J. a T., and Callaway, E.M. (2007). Monosynaptic restriction of transsynaptic tracing from single, genetically targeted neurons. Neuron 53, 639–647.

Wickersham, I.R., Sullivan, H. a, Seung, H.S., 2010. Production of glycoprotein-deleted rabies viruses for monosynaptic tracing and high-level gene expression in neurons. Nat. Protoc. 5, 595–606.

Yarmolinsky, D.A., Peng, Y., Pogorzala, L.A., Rutlin, M., Hoon, M.A., and Zuker, C.S. (2016). Coding and Plasticity in the Mammalian Thermosensory System. Neuron *92*, 1079–1092.

Zampieri, N., and de Nooij, J.C. (2020). Regulating muscle spindle and Golgi tendon organ proprioceptor phenotypes. Curr. Opin. Physiol.10.1016/j.cophys.2020.11.001.

Zampieri, N., Jessell, T.M., and Murray, A.J. (2014). Mapping Sensory Circuits by Anterograde Transsynaptic Transfer of Recombinant Rabies Virus. Neuron *81*, 766–778.

Zhang, Y., Zhao, S., Rodriguez, E., Takatoh, J., Han, B.-X., Zhou, X., and Wang, F. (2015). Identifying local and descending inputs for primary sensory neurons. J. Clin. Invest. *125*, 3782–3794.

Figure Legends

Figure 1. Retrograde infection of primary somatosensory neurons and anterograde monosynaptic spread into spinal neurons.

A) Schematics representing the strategy for genetic targeting of G and TVA expression in DRG neurons and monosynaptic tracing with pseudotyped rabies injection in the spinal cord. SN, sensory neurons; IN, interneurons; MN, motor neurons; 1, primary infection; 2, secondary transduction.

B) Parvalbumin expression in GFP$^+$ sensory neurons in p9 *PV*^{HTB} mice. Scale bar 50 µm.

C) Specificity of genetic tracing with the *PV*^{HTB} line expressed as a percentage of GFP$^+$ sensory neurons labeled by parvalbumin staining.

D) Rabies expression (mCherry) in GFP$^+$ sensory neurons at p16 after RVΔG-mCherry/EnvA injection in p9 *PV*^{HTB} mice. Scale bar 50 µm.

E) Specificity of sensory neurons targeting expressed as a percentage of RV$^+$ sensory neurons labeled by nuclear GFP after RVΔG-mCherry/EnvA injection in *PV*^{HTB} mice.

F) Efficiency of sensory neurons targeting expressed as a percentage of GFP$^+$ sensory neurons labeled by mCherry after RVΔG-mCherry/EnvA injection in *PV*^{HTB} mice.

G) Rabies expression (mCherry) in spinal neurons at p16 after RVΔG-mCherry/EnvA injection in p9 *PV*^{HTB} mice. Arrows points to motor neurons in the ventral spinal cord. Scale bar 200 µm.

H) Tomato labeling of proprioceptive sensory afferents in the spinal cord of *PV::Cre*$^{+/-}$*; Ai14*$^{f/+}$mice. Scale bar 200 µm.

I) Representative images of VGLUT1$^+$; RV$^+$ presynaptic inputs in proximity or juxtaposed to RV$^+$ interneurons (I') and motor neurons (I”) after RVΔG-mCherry/EnvA injection in *PV*^{HTB} mice. Scale bars: 200 and 20 µm (I' and I'').

Figure 2. Rabies tracing of spinal proprioceptive circuits.

A) Rabies expression (mCherry) in spinal interneurons and ChAT$^+$ motor neurons (A') after RVΔG-mCherry/EnvA injection in *PV*^{HTB} mice. Scale bars: 200 and 20 µm (A').

B) Digital reconstruction of RV$^+$ interneuron positions in *PV*^{HTB} experiments. IN, interneurons.

C) Digital reconstruction of RV$^+$; ChAT$^+$ motor neuron positions in *PV*^{HTB} experiments. MN, motor neurons.

D) Dorso-ventral (top) and medio-lateral (bottom) density analyses of RV$^+$ interneurons (top) and RV$^+$; ChAT$^+$ motor neurons (bottom) in three *PV*^{HTB} experiments.

E) Number of starter cells defined as GFP$^+$; RV$^+$ sensory neurons in *PV*^{HTB} experiments.

F) Number of spinal neurons traced in *PV*^{HTB} experiments. IN, interneurons; MN, motor neurons.

G) Connectivity index, the average number of second order neurons traced from a single starter cell in *PV*^{HTB} experiments.

H) Correlation analysis of interneurons and motor neurons positional coordinates in *PV*^{HTB} experiments (“IN vs IN” $R \geq 0.9$; “MN vs MN” $R \geq 0.8$). Scale bar indicates correlation values. IN, interneurons; MN, motor neurons.

Figure 3. Subtype identities of post-sensory neurons labeled in *PV*^{HTB} experiments.

A-D) Representative images of RV$^+$; Chx10$^+$ (V2a; A), RV$^+$; FoxP2$^+$ (V1; B), RV$^+$; Lhx1$^+$ (V0/dI4; C) and RV$^+$; calbindin$^+$ (D) interneurons labeled in *PV*^{HTB} experiments. Scale bars: 200 and 20 (high magnifications) μm.

Figure 4. Rabies tracing of spinal thermosensitive circuits.

A and B) Rabies expression (mCherry) in GFP$^+$ sensory neurons labeled after RVΔG-mCherry/EnvA injection in *TRPV1*^{HTB} (A) and *TRPM8*^{HTB} (B) mice. Scale bars 50 μm.

C) Specificity of sensory neurons targeting expressed as a percentage of RV$^+$ sensory neurons labeled by nuclear GFP after RVΔG-mCherry/EnvA injection in *TRPV1*^{HTB} and *TRPM8*^{HTB} mice.

D) Efficiency of sensory neurons targeting expressed as a percentage of GFP$^+$ sensory neurons labeled by mCherry after RVΔG-mCherry/EnvA injection in *TRPV1*^{HTB} and *TRPM8*^{HTB} mice.

E and F) RV$^+$ (mCherry) spinal neurons after RVΔG-mCherry/EnvA injection in *TRPV1*^{HTB} (E) and *TRPM8*^{HTB} (F) mice. Scale bars 200 μm.

G and H) Digital reconstruction of RV$^+$ interneuron positions in *TRPV1*^{HTB} (G) and *TRPM8*^{HTB} (H) experiments.

I) Number of starter cells defined as GFP$^+$; RV$^+$ sensory neurons in *TRPV1*^{HTB} and *TRPM8*^{HTB} experiments.

J) Number of spinal neurons traced in *TRPV1*^{HTB} and *TRPM8*^{HTB} experiments.

K) Connectivity index defined as the average number of second order neurons traced from a single starter cell in *TRPV1*^{HTB} and *TRPM8*^{HTB} experiments.

Figure 5. Organization of sensory circuits for mechanical and thermal sensation in the spinal cord.

A) Transverse contour density plots (left) and relative distribution (right) of post-sensory neurons in the dorsal (300 to 600µm), intermediate (0 to 300µm), ventral (0 to -600µm) and contralateral spinal cord of *PV*^{HTB} (interneurons: black; motor neurons: green), *TRPV1*^{HTB} (Red), and *TRPM8*^{HTB} (Blue) experiments.

B) Correlation analysis of post-sensory neurons Cartesian coordinates in *PV*^{HTB}, *TRPV1*^{HTB} and *TRPM8*^{HTB} experiments ("*TRPV1*^{HTB} vs *TRPM8*^{HTB}" $r \geq 0.85$; "*TRPV1*^{HTB}or *TRPM8*^{HTB} vs *PV*^{HTB}" $r \leq 0.55$). Scale bar indicates correlation values.

C) PKCγ and mCherry expression on ipsilateral dorsal spinal cords after RVΔG-mCherry/EnvA injection in *PV*^{HTB}, *TRPV1*^{HTB}, and *TRPM8*^{HTB} mice. Scale bar 200 µm.

D) Digital reconstruction of RV^{+} interneuron positions in the dorsal spinal cord of *PV*^{HTB} (black), *TRPV1*^{HTB} (red), and *TRPM8*^{HTB} experiments.

E) Box-plot showing the dorso-ventral distributions of RV^{+} interneurons in the dorsal horn of *PV*^{HTB} (black), *TRPV1*^{HTB} (red), and *TRPM8*^{HTB} (blue) experiments. PKCγ staining (white) is used as an internal reference.

F) CGRP and mCherry expression on ipsilateral dorsal spinal cords after RVΔG-mCherry/EnvA L1 injection in *PV*^{HTB}, *TRPV1*^{HTB}, and *TRPM8*^{HTB} mice. Scale bar 200 µm.

G) Percentage of RV^{+} neurons found in CGRP (laminae I-IIo) and PKCγ (laminae IIi-III) areas in *PV*^{HTB}, *TRPV1*^{HTB}, and *TRPM8*^{HTB} experiments.

Supplementary Figure Legends

Figure S1. Specific labeling of proprioceptive neurons with PV^{HTB} mouse line.

A) Representative images of lumbar sections showing GFP$^+$ sensory neurons in the DRG of p10 PV^{HTB} mice. Scale bar 200 μm.

B) Examples of RV$^+$; GFP$^+$; PV$^+$ sensory neurons after RVΔG-mCherry/EnvA L1 injection in PV^{HTB} mice. Scale bar 50 μm.

C) Representative images of lumbar DRG and spinal cord sections showing RV$^+$; GFP$^+$ sensory neurons and absence of transsynaptic labeling after RVΔG-mCherry/EnvA L1 injection in $PV::cre^{+/-}; HTB^{f/+}$ ($PV^{HTB\ f/+}$) mice. Scale bars :50 (DRG) and 200 μm (spinal cords).

Figure S2. Post-sensory connectivity maps from p9-p16 PV^{HTB} experiments.

A) Representative images of RV$^+$ spinal neurons after RVΔG-mCherry/EnvA L1 injection in PV^{HTB} experiments. Scale bar 200 μm.

B) Digital reconstruction of RV$^+$ neuron positions in PV^{HTB} experiments.

Figure S3. Parvalbumin interneurons labelled in p9-p16 PV^{HTB} experiments.

A) Representative images and digital reconstruction of GFP$^+$; PV$^+$ spinal interneurons positions at p16 after RVΔG-mCherry/EnvA L1 injection in p9 PV^{HTB} mice. Scale bar 200 and 20 μm (high magnification).

B) Digital reconstruction of GFP$^+$; PV$^+$ rostro-caudal position neuron positions in PV^{HTB} experiments.

Figure S4. Post-sensory connectivity maps from p9-p16 $TRPV1^{HTB}$ and $TRPM8^{HTB}$ experiments.

A and B) Representative images of parvalbumin and tdTomato labeling of somatosensory neurons cell bodies and afferents in the DRG and spinal cords of p9 $TRPV1::Cre^{+/-}; Ai14^{f/+}$ (C) and $TRPM8::Cre^{+/-}; Ai14^{f/+}$ mice. Scale bars 200 μm.

C) Representative images of *Trpv1* and *Trpm8* mRNA expression in DRG sensory neurons in p16 $TRPV1^{HTB}$ mice. Scale bar 50 μm.

D) Quantification of GFP$^+$ neurons expressing *Trpv1* and *Trpm8,* in p16 $TRPV1^{HTB}$ mice (n=3, average +/- SEM).

E) Digital reconstruction of RV$^+$ neuron positions in $TRPV1^{HTB}$ (Top, red)) and $TRPM8^{HTB}$ (Bottom, blue) experiments.

F) Correlation analysis of post-sensory neurons Cartesian coordinates in *TRPV1*^{HTB} and *TRPM8*^{HTB} experiments.

G) Dorso-ventral density plot showing the distributions of RV^{+} interneurons in the dorsal horn of *PV*^{HTB} (black), *TRPV1*^{HTB} (red) and *TRPM8*^{HTB} (blue) experiments.

Figure S5. Rabies tracing from p30-p37 *TRPV1*^{HTB} and *TRPM8*^{HTB} experiments.

A and B) Rabies expression (mCherry) in GFP^{+} sensory neurons labeled after RVΔG-mCherry/EnvA injection in p30 *TRPV1*^{HTB} (A) and *TRPM8*^{HTB} (B) mice. Scale bars 100μm.

C and D) RV^{+} (mCherry) spinal neurons after RVΔG-mCherry/EnvA injection in p30 *TRPV1*^{HTB} (E) and *TRPM8*^{HTB} (F) mice. Scale bars 200 μm.

E and F) Digital reconstruction of RV^{+} interneuron positions in *TRPV1*^{HTB} (E) and *TRPM8*^{HTB} (F) experiments.

G) Dorso-ventral density plots showing the distributions of RV^{+} interneurons in the dorsal horn of *TRPV1*^{HTB} (red) and *TRPM8*^{HTB} (blue) experiments.

H) Number of spinal neurons traced in *TRPV1*^{HTB} and *TRPM8*^{HTB} experiments.

Figure 1

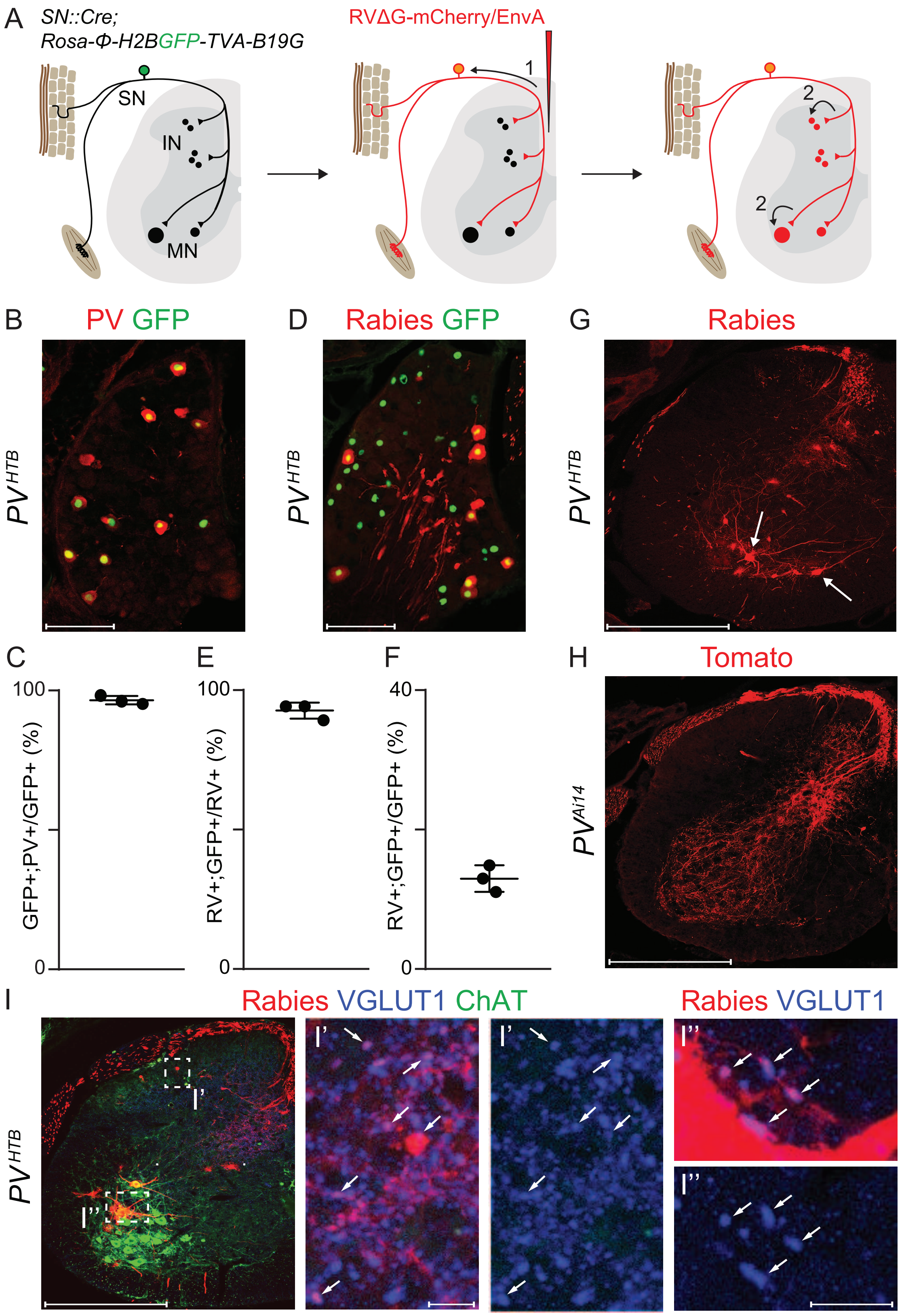
A
SN::Cre;
Rosa-Φ-H2BGFP-TVA-B19G
SN
IN
MN
RVΔG-mCherry/EnvA
1
2
2
B
PV GFP
PV HTB
D
Rabies GFP
PV HTB
G
Rabies
PV HTB
C
100
0
GFP+;PV+/GFP+ (%)
E
100
0
RV+;GFP+/RV+ (%)
F
40
0
RV+;GFP+/GFP+ (%)
H
Tomato
PV Ai14
I
Rabies VGLUT1 ChAT
PV HTB
I'
I''
I'
I'
Rabies VGLUT1
I''
I''

Figure 2

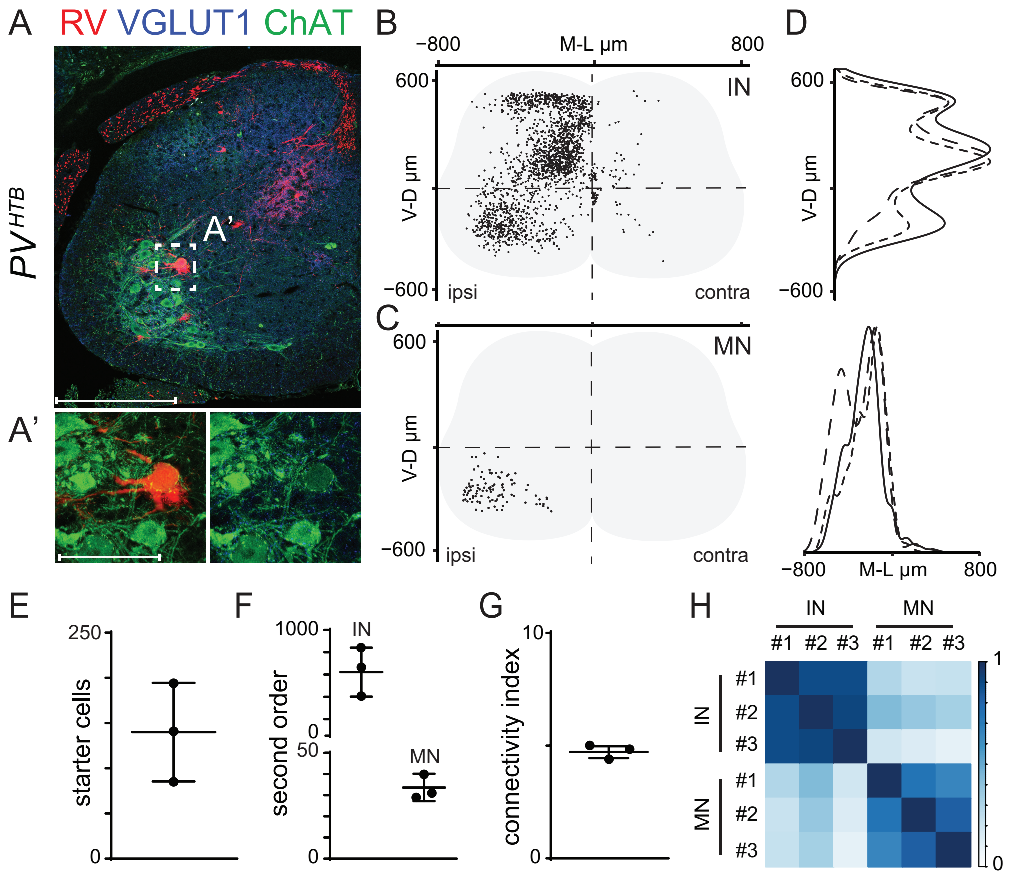
A
RV VGLUT1 ChAT
PV^HTB
A'
A'
B
−800
M-L µm
800
600
−600
V-D µm
IN
ipsi
contra
C
600
−600
V-D µm
MN
ipsi
contra
D
600
−600
V-D µm
−800
M-L µm
800
E
250
0
starter cells
F
1000
0
50
0
IN
MN
second order
G
10
0
connectivity index
H
IN
MN
#1 #2 #3 #1 #2 #3
IN
#1
#2
#3
MN
#1
#2
#3
1
0

Figure 3

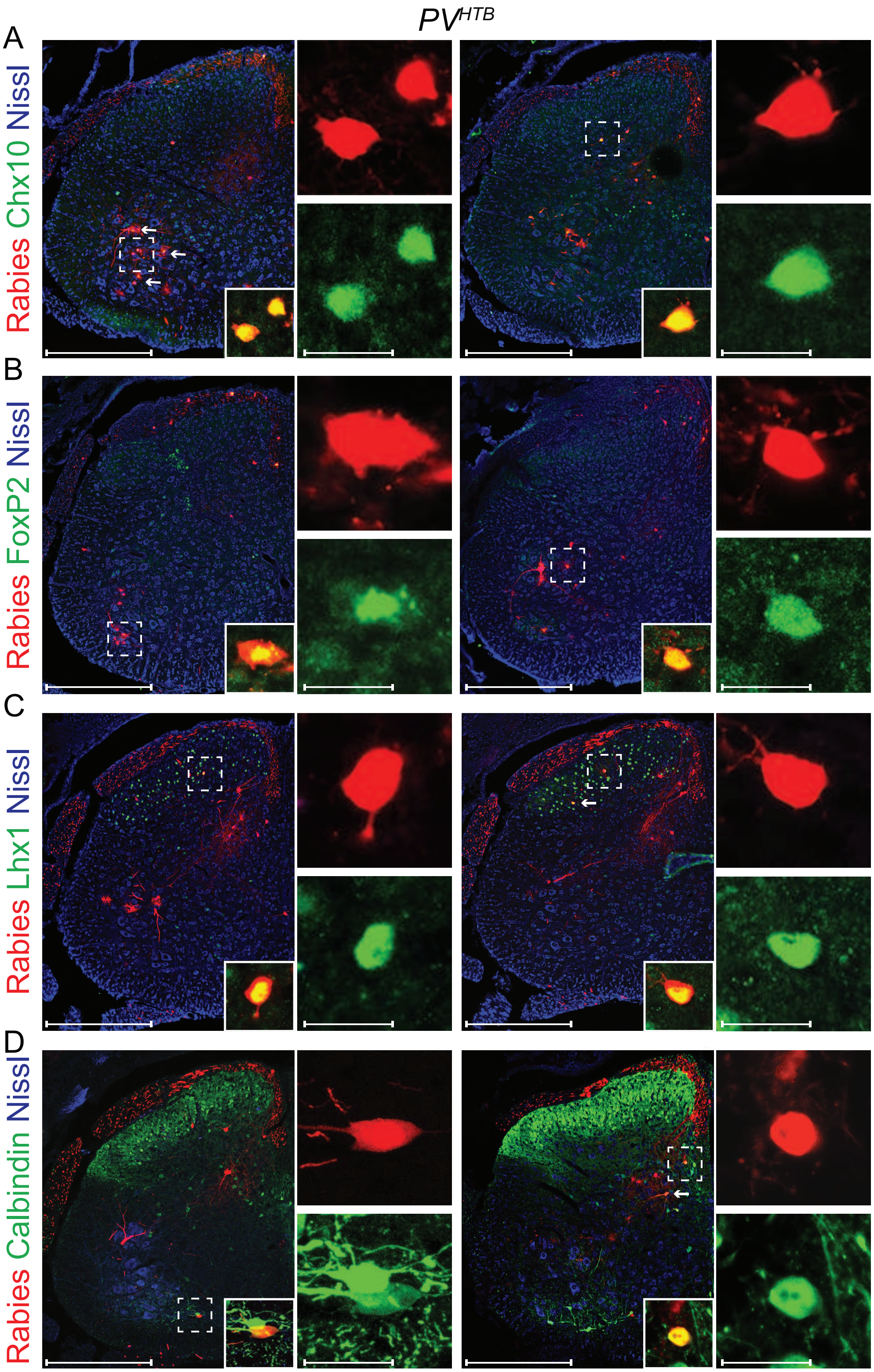
PV^{HTB}
A
Rabies Chx10 Nissl
B
Rabies FoxP2 Nissl
C
Rabies Lhx1 Nissl
D
Rabies Calbindin Nissl

Figure 4

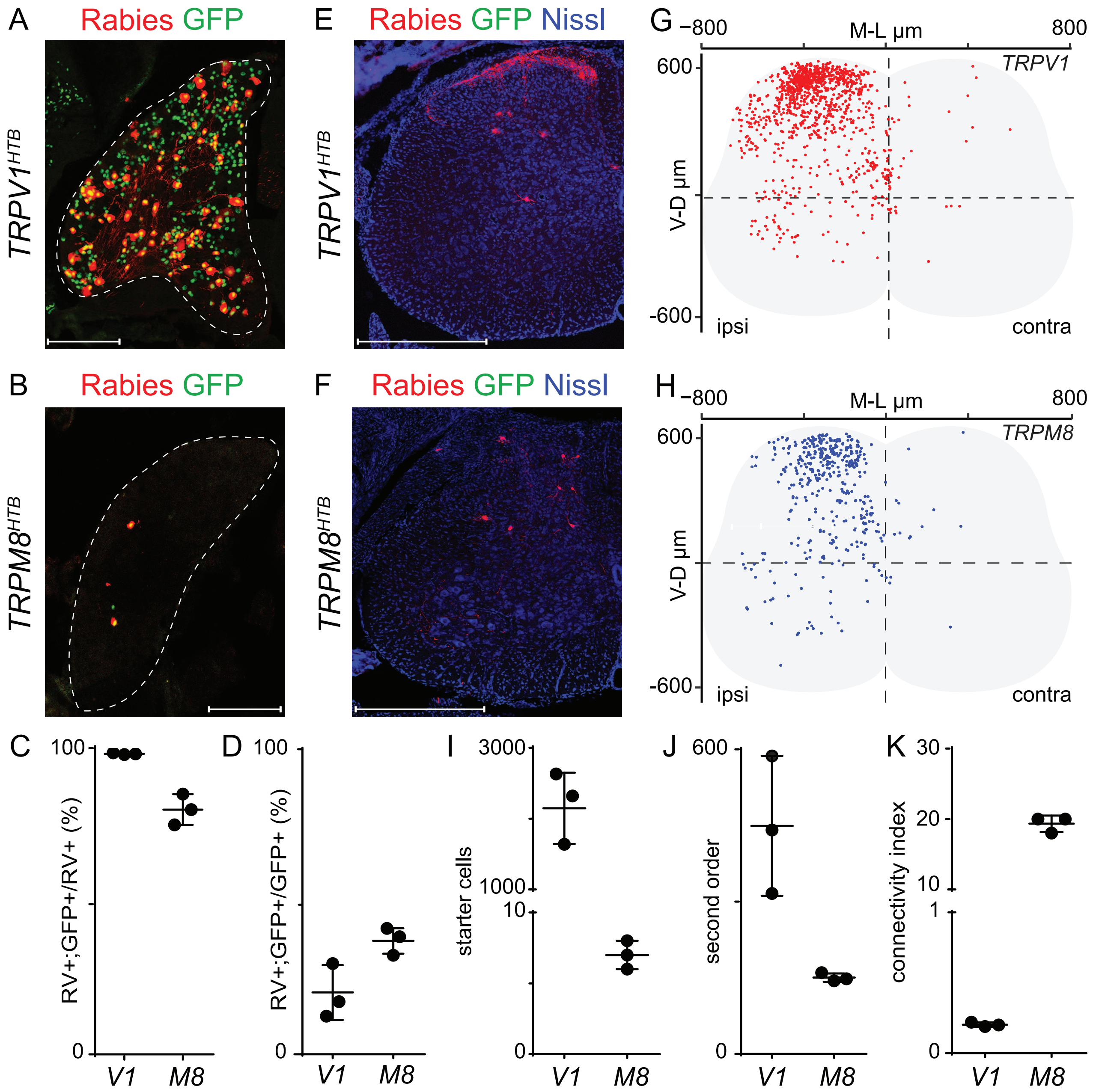
A
Rabies GFP
TRPV1^HTB
B
Rabies GFP
TRPM8^HTB
E
Rabies GFP Nissl
TRPV1^HTB
F
Rabies GFP Nissl
TRPM8^HTB
G
-800
M-L µm
800
600
TRPV1
V-D µm
-600
ipsi
contra
H
-800
M-L µm
800
600
TRPM8
V-D µm
-600
ipsi
contra
C
100
RV+;GFP+/RV+ (%)
0
V1
M8
D
100
RV+;GFP+/GFP+ (%)
0
V1
M8
I
3000
1000
10
starter cells
0
V1
M8
J
600
second order
0
V1
M8
K
30
20
10
1
connectivity index
0
V1
M8

Figure 5

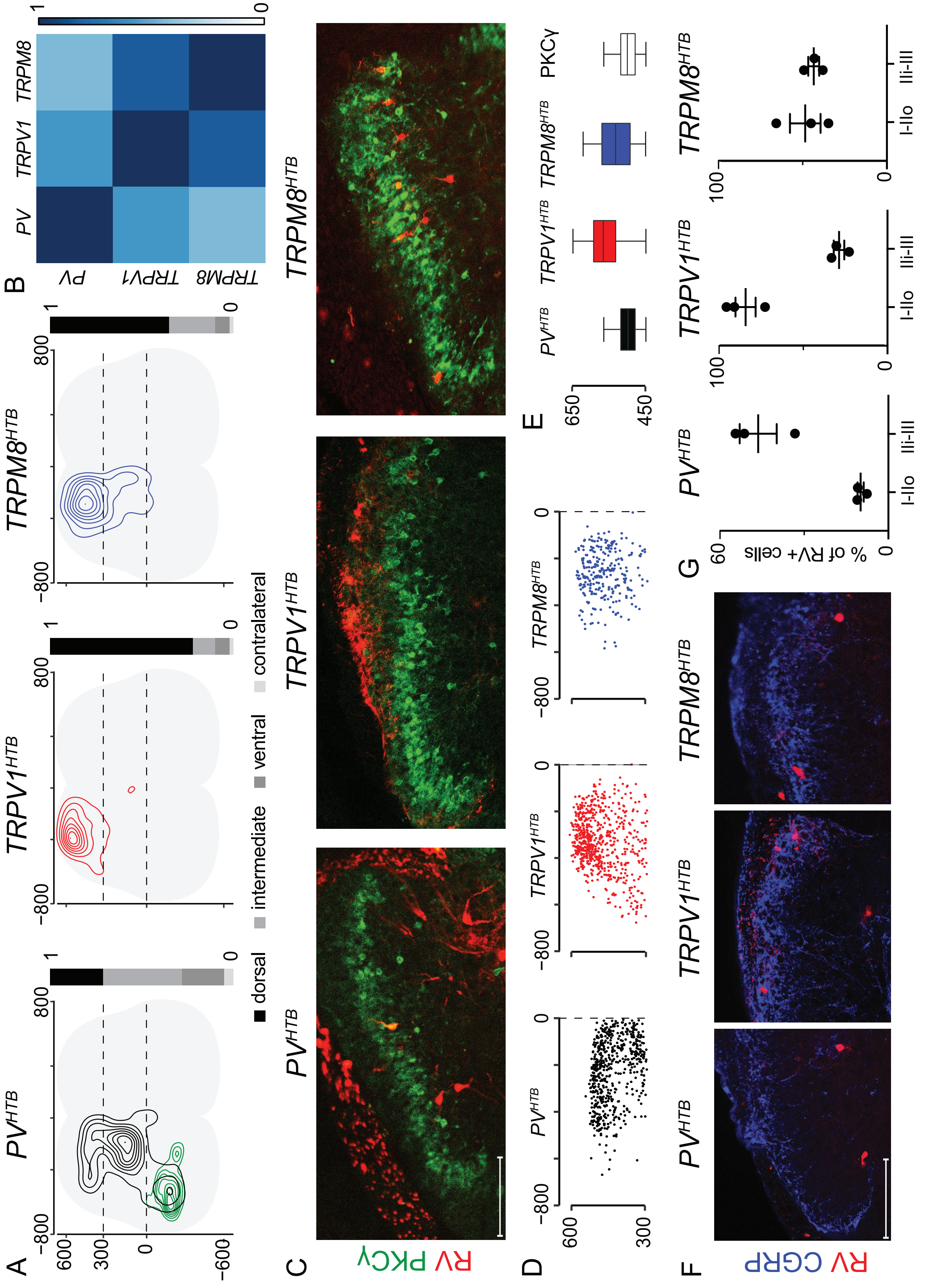
A
PV^HTB
TRPV1^HTB
TRPM8^HTB
600
300
0
−600
−800
800
1
0
dorsal
intermediate
ventral
contralateral
B
PV
TRPV1
TRPM8
1
0
C
RV PKCγ
PV^HTB
TRPV1^HTB
TRPM8^HTB
D
600
300
−800
0
E
650
450
PV^HTB
TRPV1^HTB
TRPM8^HTB
PKCγ
F
RV CGRP
PV^HTB
TRPV1^HTB
TRPM8^HTB
G
% of RV+ cells
60
100
0
I-IIo
IIi-III

Table S1

Table S1.

Line	**Genotype**	**#**	**# GFP$^+$ spinal neurons**	**# GFP$^+$; RV$^+$ spinal neurons**	**# of starter cells**	**# of RV$^+$ Spinal neurons**	**Specificity (%)**	**Efficiency (%)**	**Connectivity index**
PV^{HTB}	*PV:: cre +/-; Rosa-HTB f/f*	*1*	996	4	85	413	89	12	4.86
		2	780	3	141	696	94	14	4.94
		3	1292	3	194	858	94	16	4.42
TRPV1^{HTB}	*TRPV1::cre+/-; Rosa-HTB f/f*	*1*	0	0	2939	545	98	17	0.19
		2	0	0	1580	302	98	30	0.19
		3	0	0	1642	312	98	13	0.19
TRPM8^{HTB}	*TRPM8::cre+/-; Rosa-HTB f/f*	*1*	0	0	7	139	75	40	19.86
		2	0	0	8	154	85	38	19.25
		3	0	0	7	143	80	32	20.42

Click here to access/download

Supplementary Material - Video(s)

Movie 1.mp4

Supplemental Figure 1

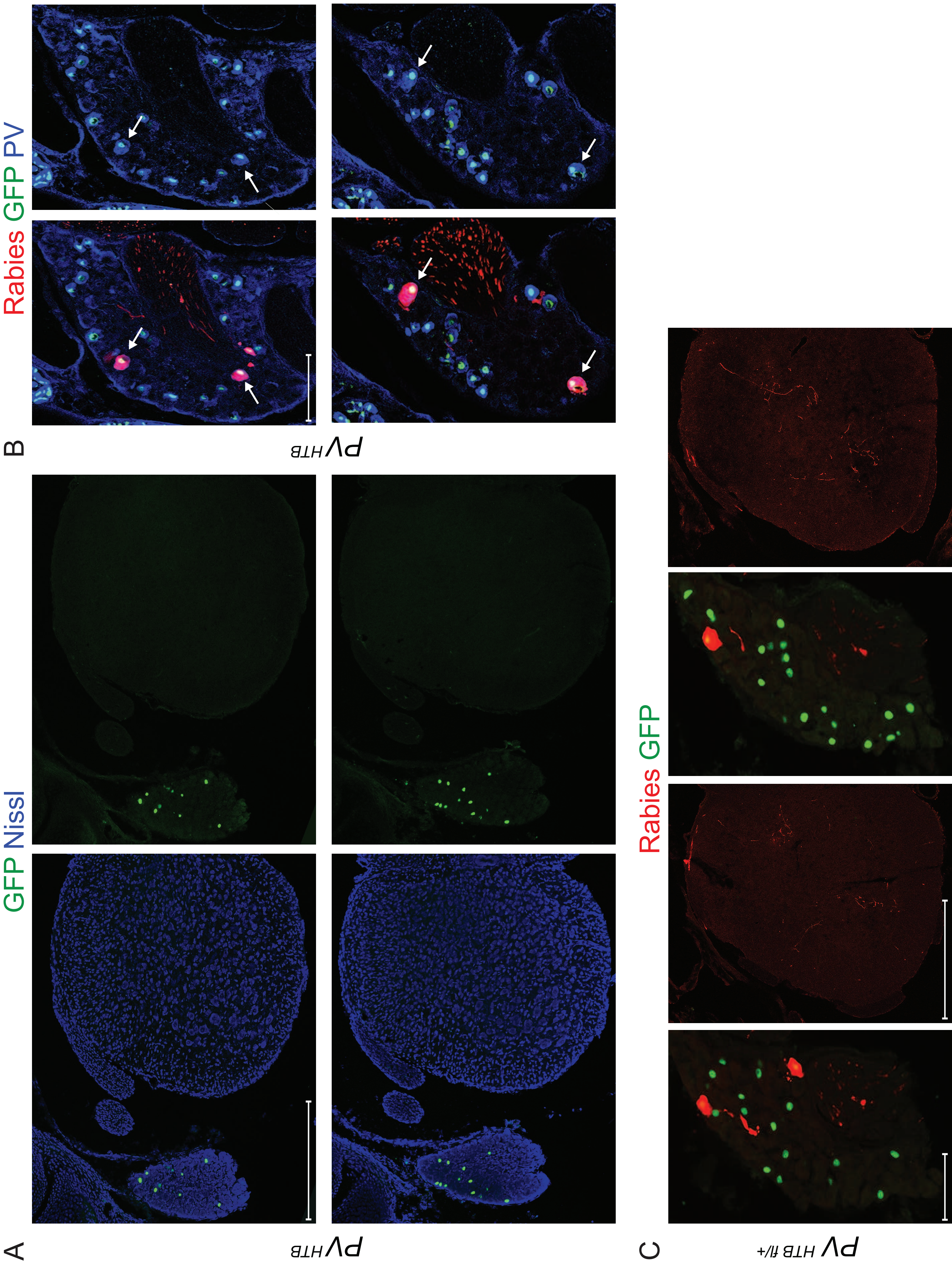
B
Rabies GFP PV
PV HTB
A
GFP Nissl
PV HTB
C
Rabies GFP
PV HTB fl/+

Supplemental Figure 2

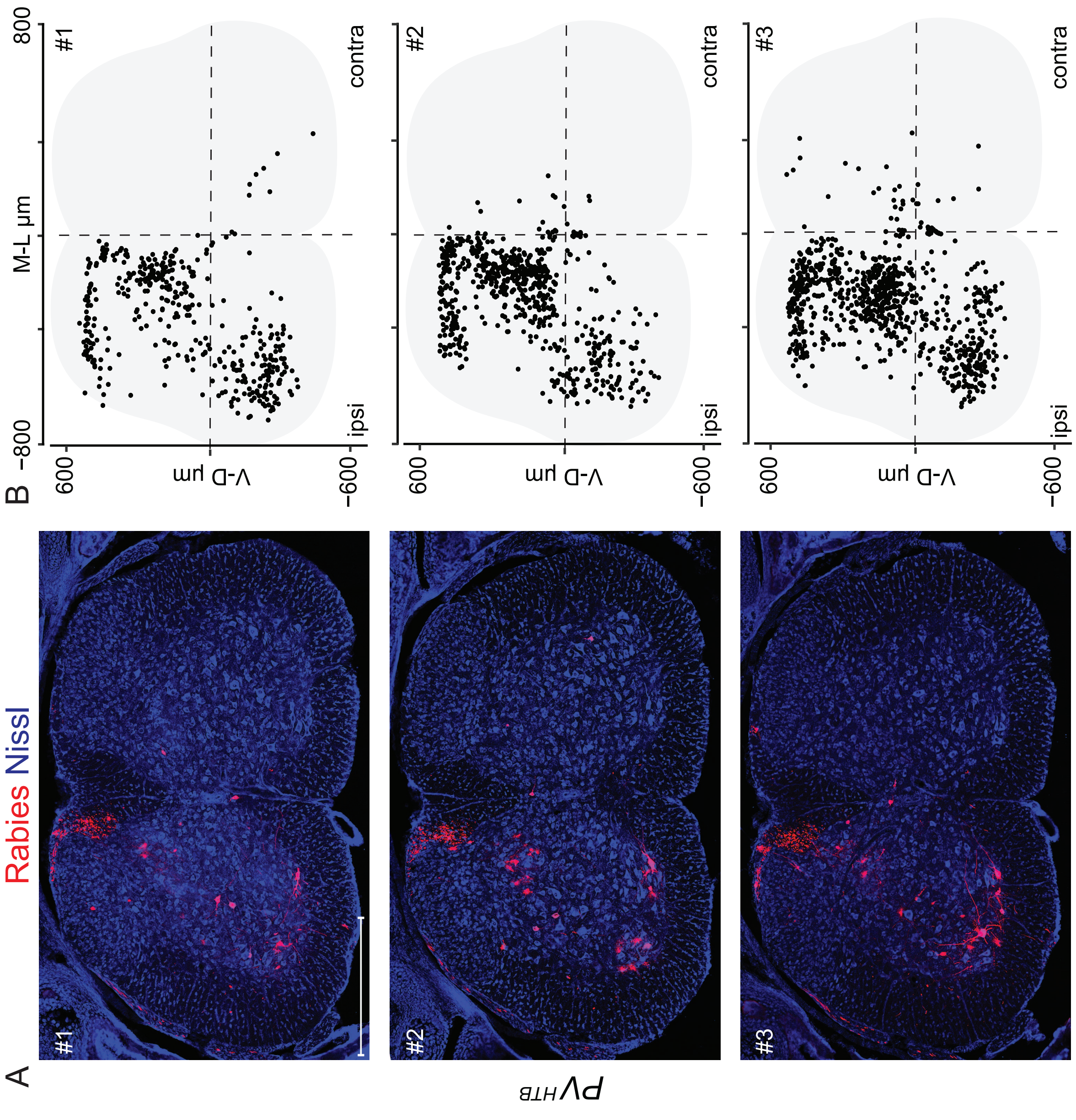
A
Rabies Nissl
#1
#2
#3
PV_{HTB}
B
M-L µm
−800
800
V-D µm
600
−600
#1
#2
#3
contra
ipsi

Supplemental Figure 3

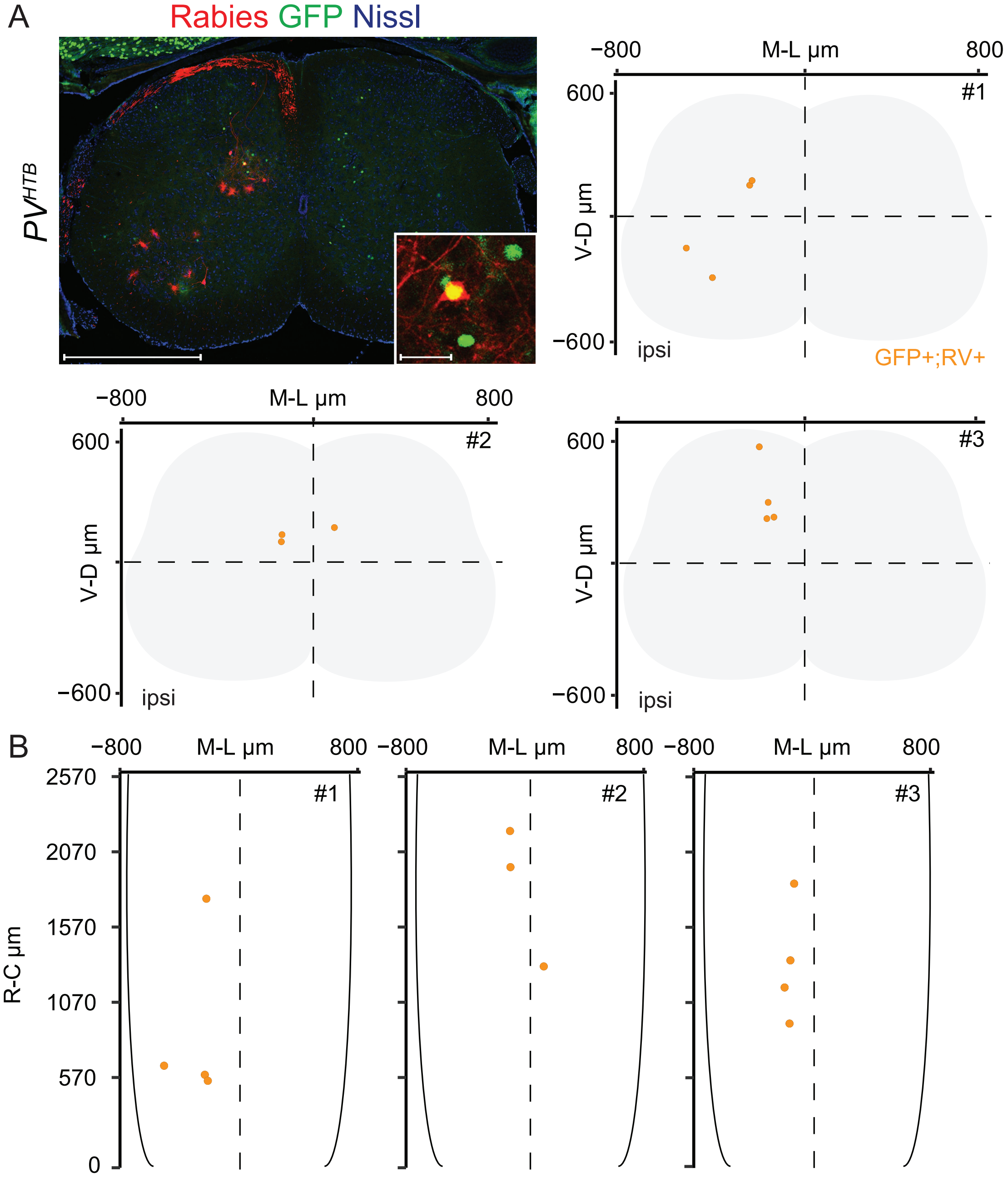

Supplemental Figure 4

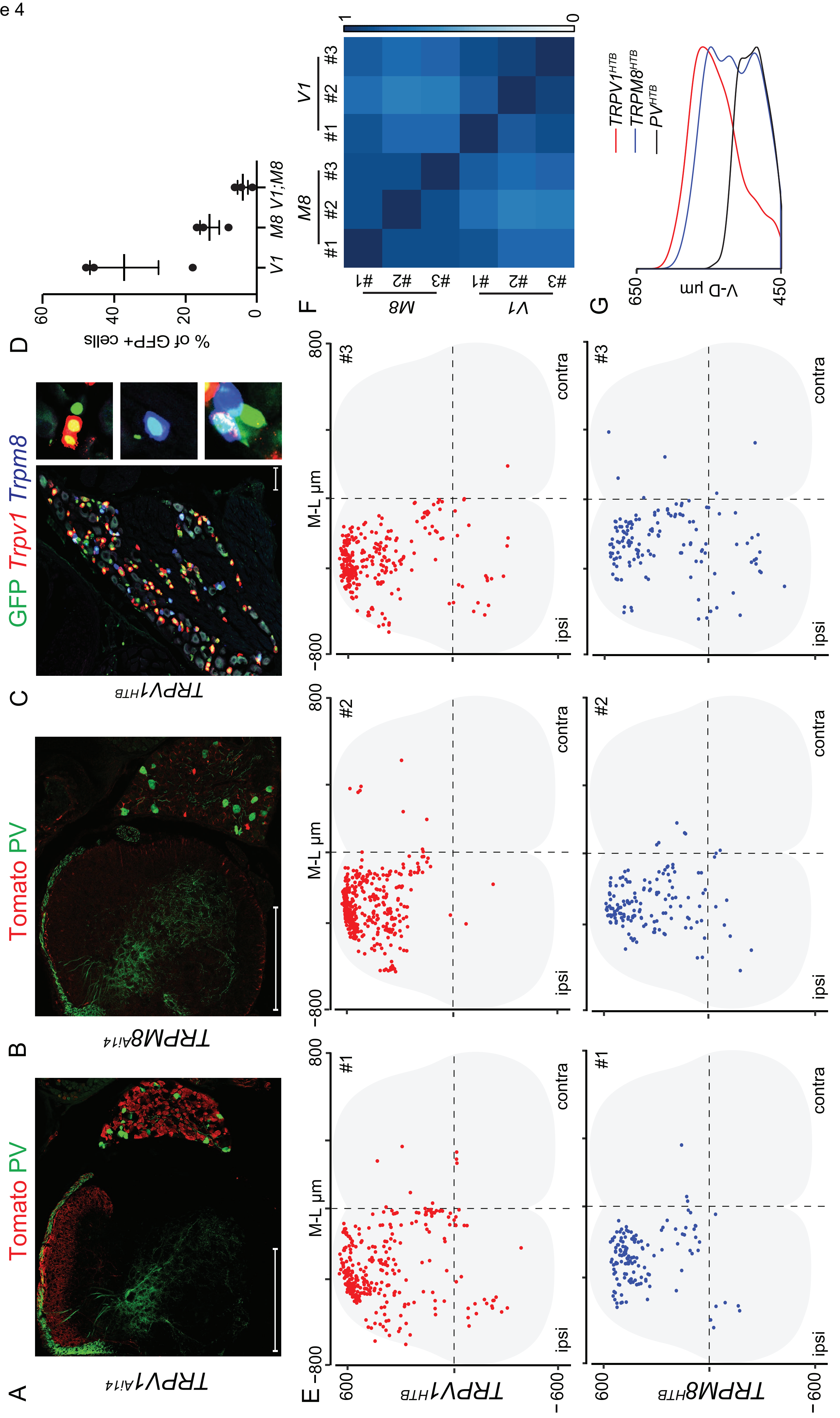

Supplemental Figure 5

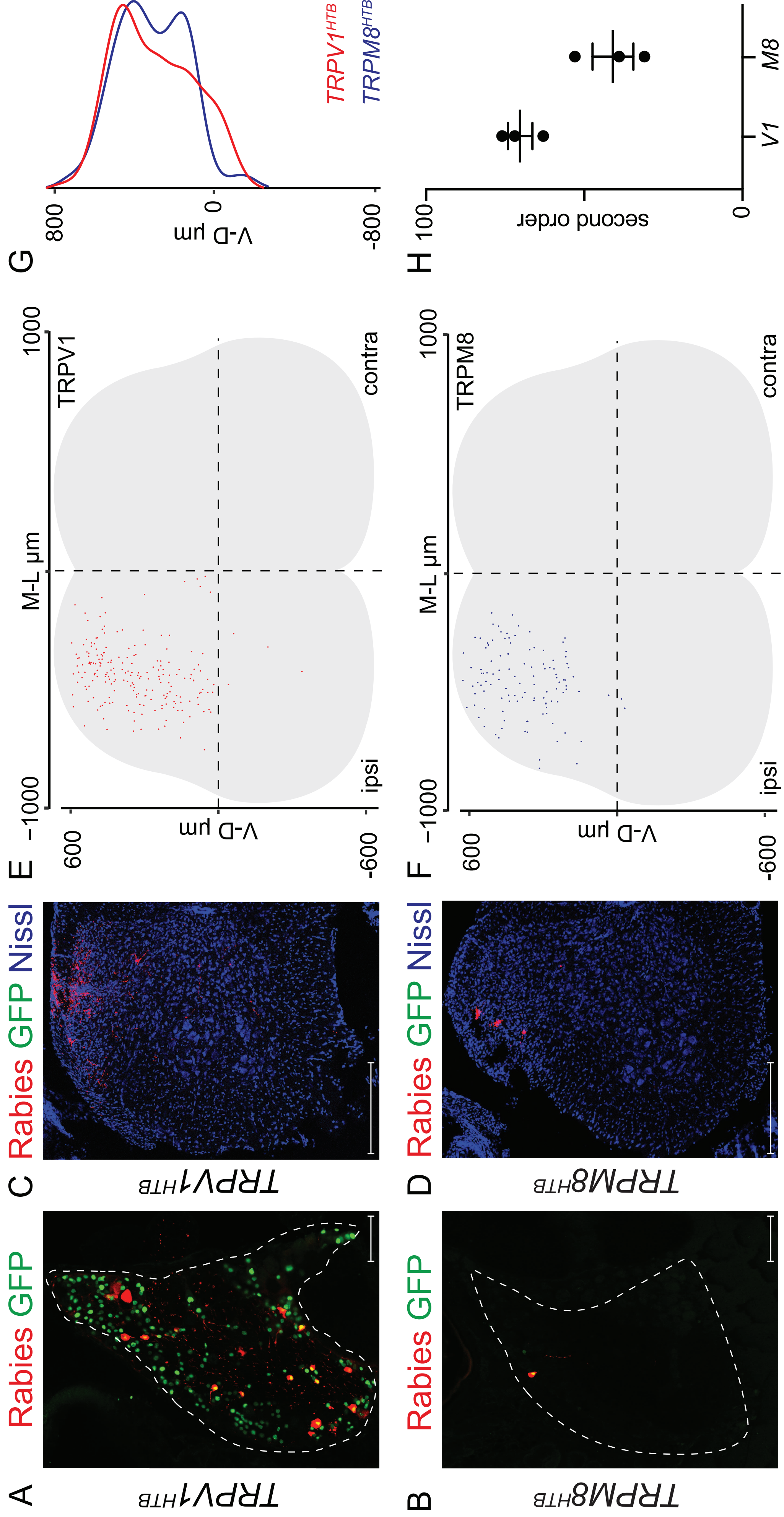
A
TRPV1HTB
Rabies GFP
B
TRPM8HTB
Rabies GFP
C
TRPV1HTB
Rabies GFP Nissl
D
TRPM8HTB
Rabies GFP Nissl
E
TRPV1
M-L µm
−1000
1000
600
V-D µm
-600
ipsi
contra
F
TRPM8
M-L µm
−1000
1000
600
V-D µm
-600
ipsi
contra
G
800
0
-800
V-D µm
TRPV1HTB
TRPM8HTB
H
100
0
second order
V1
M8